Plasma Physics and Controlled Fusion

PAPER

Study of Stark broadening of krypton helium-β lines and estimation of electron density and temperature in NIF compressed capsules

To cite this article: K W Hill *et al* 2022 *Plasma Phys. Control. Fusion* **64** 105025

View the article online for updates and enhancements.

You may also like

- A Parameter Space Exploration of High-resolution Numerically Evolved Early Type Galaxies Including AGN Feedback and Accurate Dynamical Treatment of Stellar Orbits
Luca Ciotti, Jeremiah P. Ostriker, Zhaoming Gan et al.
- Optimization of thermal oxidation for 4H-SiC and fabricate/characterize MOS capacitor
Rajesh Singh Shekhawat, Nongthombam Joychandra Singh, Moh. Shakil et al.
- PZT/PLZT - elastomer composites with improved piezoelectric voltage coefficient
K. Harikrishnan, D V Bavbande, Dhirendra Mohan et al.

IOP ebooks™

Bringing together innovative digital publishing with leading authors from the global scientific community.

Start exploring the collection–download the first chapter of every title for free.

This content was downloaded from IP address 176.230.227.191 on 26/09/2022 at 12:36

IOP Publishing Plasma Physics and Controlled Fusion
Plasma Phys. Control. Fusion **64** (2022) 105025 (11pp) https://doi.org/10.1088/1361-6587/ac9017

Study of Stark broadening of krypton helium-β lines and estimation of electron density and temperature in NIF compressed capsules

K W Hill[1,*], L Gao[1], B F Kraus[1], M Bitter[1], P C Efthimion[1], N Pablant[1], M B Schneider[2], D B Thorn[2], H Chen[2], R L Kauffman[2], D A Liedahl[2], M J MacDonald[2], A G MacPhee[2], H A Scott[2], S Stoupin[2], R Doron[3], E Stambulchik[3], Y Maron[3] and B Lahmann[4]

[1] Princeton Plasma Physics Laboratory, Princeton, NJ 08543, United States of America
[2] Lawrence Livermore National Laboratory, Livermore, CA 94550, United States of America
[3] Weizmann Institute of Science, Rehovot 7610001, Israel
[4] Massachusetts Institute of Technology, Cambridge, MA 02139, United States of America

E-mail: khill@pppl.gov

Received 8 March 2022, revised 17 August 2022
Accepted for publication 7 September 2022
Published 19 September 2022

Abstract

The National Ignition Facility (NIF) diagnostic instrument manipulator (DIM) - based high resolution (dHIRES) x-ray spectrometer was used to measure the time evolution of the electron density (n_e) and temperature (T_e) in the hot spot of four NIF compressed capsules with 25 ps time resolution during the 'stagnation' phase. The electron density was inferred by comparing the measured Stark broadening of the krypton (Kr) Heβ spectral complex with theoretical calculations that include ion dynamic effects, and the electron temperature was inferred by comparing the measured ratio of the intensity of a dielectronically excited Li-like Kr line to the intensity of the Kr Heβ resonance line with calculations using the spectroscopic collisional radiative atomic model (SCRAM) and CRETIN collisional-radiative models. The inferred, time averaged n_e values mainly agree with n_e values from neutron diagnostics within uncertainties, but the neutron time-of-flight values of T_{ion} are consistently higher than dHIRES T_e values by 200–700 eV. The dHIRES measurements and measurement techniques, method of uncertainty analysis, and discussion of comparisons with measurements from neutron diagnostics are presented.

Keywords: x-ray, spectroscopy, inertial confinement fusion, plasma parameters

(Some figures may appear in colour only in the online journal)

1. Introduction

In laser driven inertial confinement fusion (ICF) the fuel is contained inside a capsule which is rapidly heated and spherically compressed by a powerful laser driver to a stagnated plasma in a central 'hot spot' with fusion relevant density and temperature conditions [1, 2]. The compression process converts pressure times change in volume (PdV) work to internal energy and, ultimately, into thermal energy, heating the fuel, and the fuel density is greatly increased owing to a large decrease in the volume of the capsule. In the stagnated phase the conditions are still evolving due to the continued conversion of mechanical energy to thermal energy; therefore, accurate time resolved measurements of the hot-spot plasma parameters are important for assessing the implosion performance toward understanding how to achieve ignition [2, 3].

* Author to whom any correspondence should be addressed.

 © 2022 IOP Publishing Ltd

The temperature and pressure in an ignition capsule near the stagnation time indicate the quality of the implosion [4]. Most current techniques for measuring hot spot temperature and density are time-integrated and, therefore, do not elucidate the evolution of the hot spot parameters during the stagnation phase. Presently, the pressure is deduced from neutron-based measurements of the temperature and density [5, 6]. The ion temperature, $T_{\rm ion}$, is typically measured from the neutron Doppler broadening, which is complicated by plasma flows [7, 8]. The density is deduced from $T_{\rm ion}$, the neutron yield, the size of the hotspot, and the duration of the burn, assuming uniform plasma conditions [9]. The electron temperature is inferred from the x-ray continuum spectrum by multiple detectors with absorber foils of different thicknesses [10, 11] or, more recently, by using a highly annealed pyrolytic graphite conical crystal spectrometer (ConSpec for continuum spectrometer) [12, 13] recording the continuum spectrum dispersed onto an image plate (IP). The ConSpec spectrometer is designed to ultimately provide a time history of $T_{\rm e}$ by recording the spectra on the photocathode of an x-ray streak camera, but it has only been used to date in the time-integrated mode.

To provide time-resolved measurements of the electron temperature and density of the hot spot during the stagnation phase, a moderately high resolution ($E/\Delta E \sim 1300$), absolutely calibrated, time resolving x-ray spectrometer [14, 15] has been installed at the National Ignition Facility (NIF) and has been operated during four NIF shots. The electron temperature, $T_{\rm e}$, and density, $n_{\rm e}$, were measured with x-ray spectroscopy by doping a surrogate capsule with a very small amount of krypton (Kr) gas. Because the hot spot likely equilibrates quickly, $T_{\rm e} = T_{\rm ion}$, a measurement of $T_{\rm e}$ can be used to check the neutron measurements of $T_{\rm ion}$. Another goal in fielding the new, high resolution spectrometer was to benchmark in deuteron-deuteron (DD) implosions the continuum spectrometer (ConSpec [12]) which was built to measure the electron temperature in an igniting capsule (which has no Kr) from the slope of the continuum x-ray emission.

Preliminary results of some of the measurements made for three of the four NIF shots have been provided by Gao *et al* [2]. The spectrometer is called diagnostic instrument manipulator (DIM) - based high resolution (dHIRES), for the Diagnostic Instrument Manipulator (DIM) HIgh RESolution spectrometer, and provides time-resolved measurements of Kr Heα ($1s^2$–$1s2p$) and Heβ ($1s^2$–$1s3p$) spectra with a time resolution of approximately 25 ps. The purpose of the spectrometer is to provide a measurement of electron density ($n_{\rm e}$) and temperature ($T_{\rm e}$) in the hot spot of compressed NIF capsules, in order to provide improved physics understanding of the implosions and to corroborate the time-integrated measurement of ion temperature ($T_{\rm ion}$) and electron density inferred from neutron diagnostics [9]. With dHIRES, electron density is inferred by comparing the measured Stark broadening [16–20] of the Kr Heβ spectral complex with theoretical calculations, which include ion dynamic effects [21], of Stark broadening of the Kr Heβ spectral complex, and the electron temperature is inferred by comparing the measured ratio of intensity of a dielectronically excited Li-like Kr line to the intensity of the Kr Heβ resonance line with calculations using the spectroscopic collisional radiative atomic model (SCRAM) [22] and CRETIN [23] collisional-radiative (CR) models.

2. Methods

2.1. Stark theory and inference of dependence of Stark line shape parameters on density, electric microfield strength

The process of inferring the electron density of the compressed capsules involves comparing the measured Kr Heβ line shapes with the line shapes predicted by a theoretical model. Kr Heβ line shapes or 'profiles' from a model known as SimU, developed by Stambulchik and Maron [21], are illustrated in figure 1. The curves are profiles calculated for an electron temperature ($T_{\rm e}$) of 3000 eV with various electron densities, ($n_{\rm e}$), as a function of x-ray energy relative to the unperturbed energy of 15.435 keV [24].

In the SimU code, the level energies are taken from the National Institute of Science and Technology (NIST) database [25] and the radius-vector matrix elements calculated by the cFAC (in programming language C) code [26], which is based on the flexible atomic code (FAC) [27]. The paper of Rosmej *et al* [20] includes a comparison with FAC and the relevant matrix elements agree quite well.

From these curves it can be seen that as the electron density increases, the lineshape broadens; the amplitudes of the low and high energy peaks relative to that of the central peak increase; the energy of the central peak decreases; and the energy of the higher energy peak increases.

The broadening and shifts of the spectral lines illustrated in figure 1 result from the perturbation of the radiating ions due to charged particles—the Stark broadening effect. The observed effects occur when the electron and ion densities in the vicinity of the radiator become sufficiently high such that the electric microfields significantly perturb or modify the electronic structure of the radiating ion. The theory of this type of broadening can be divided into two parts [28]. The first is a calculation of the electric microfield strength near the radiator, and the second is a quantum mechanical calculation of the effect of the added potential on the electronic structure and decay rates of the radiating ion. The electric microfield distribution is calculated either by analytical theories or by detailed molecular dynamic treatment, and various approximations for treating the differing electron and ion perturber contributions have been used. In an earlier work, impact broadening by electrons and static ion models (the standard model [29]) were used. Subsequent studies indicated that the static ion approximation resulted in some significant discrepancies between theory and experiment [29, 30]. Thus, the theory of ion dynamic contributions was developed and was applied in the model used to interpret the present experiments [21]. A recent review of Stark theoretical models was provided by Gigosos [31].

Several previous studies have been conducted to measure electron density in high energy-density plasmas or compressed capsules that have been based on K-shell spectra of lower atomic number ions, Ar or Ne, and have generally used the development and use of, perhaps, less sophisticated

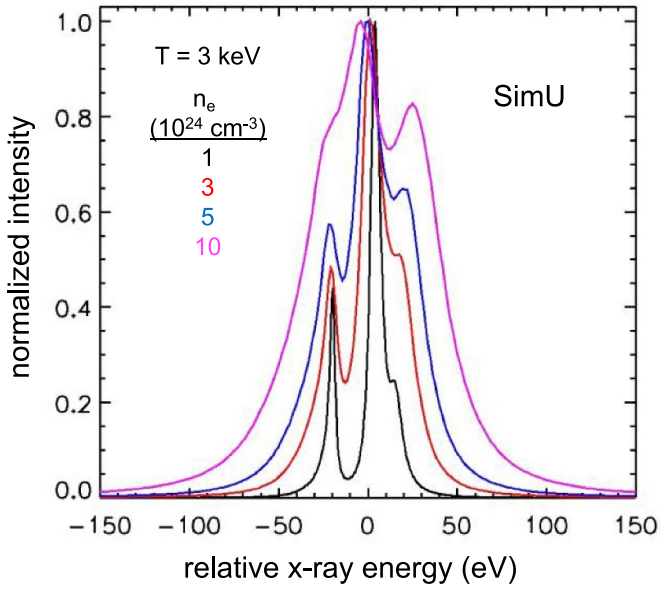

Figure 1. Theoretical Kr Heβ Stark broadened line shapes from the code SimU for different electron densities as explained in the text.

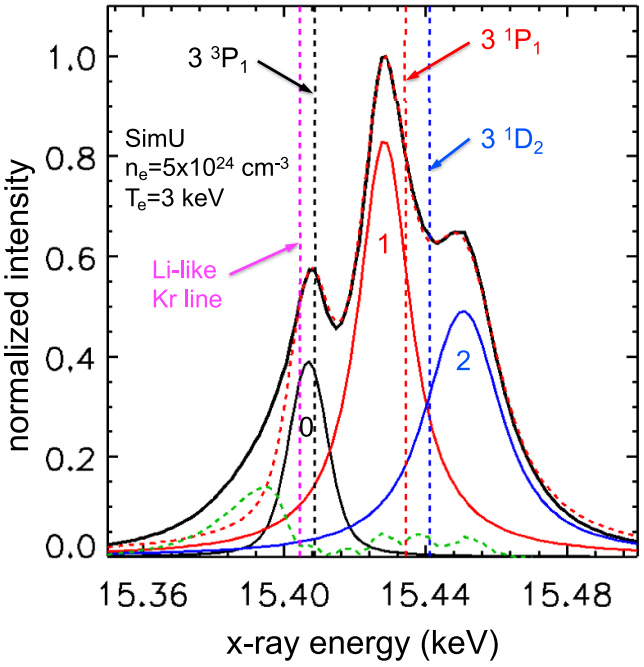

Figure 2. Approximation (red dashed curve) of theoretical Kr Heb Stark broadened line shape (solid black curve) by three Voigt profiles for $T_e = 3000$ eV and $n_e = 3 \times 10^{24}$ cm^{-3}.

broadening theory than the present work. This earlier experimental work and the underlying theory used, as well as some previous experiments, is summarized in papers by Woolsey in papers [19, 20, 29]. Other pioneering work on the effect of high density plasmas on atomic structure, line broadening and level shifts is presented in [32–35]. Woolsey experimentally measured electron densities well below and up to 10^{24} cm^{-3} and electron temperatures less than 1 keV. At these plasma parameters the optical depth of the Ar XVII Heβ transition was quoted by the authors to be in the range of 0.2–0.4, which results in a small amount of opacity or self-absorption broadening. At the NIF parameters, however, where n_e is in the range of 2×10^{24}–5×10^{24} cm^{-3} and $T_e = 3$–5 keV, the optical depth, as calculated by the FLYCHK collisional radiative code, [36] is in the range of 15–40 for the concentration of Ar used in the experiments of Woolsey (0.1 atm Ar in 50 atm of D_2, i.e. an Ar concentration of 2 x 10^{-3}).

Thus, to avoid complication of the line width measurement due to significant opacity broadening, Kr Heβ was chosen for the NIF n_e and T_e measurements, and the atomic concentration of Kr was maintained at $\sim 10^{-4}$ in order to yield a usable signal while maintaining the self-absorption at acceptable levels. At this concentration, the optical depth of Kr was calculated by FLYCHK and by SCRAM to be about 0.5 at $T_e = 3.5$ keV, $n_e = 5 \times 10^{24}$ cm^{-3}, which results in an estimated 10% of opacity broadening. A recent study of using the FLYCHK code to calculate opacities has been published by Cho *et al* [37].

Krypton K-shell Heβ spectra were chosen for the present study because the Stark broadening is relatively large; the high density plasma ($n_e \sim 2 \times 10^{24}$–$5 \times 10^{24}$ cm^{-3}) is relatively optically thin to the high energy (~15.43 keV) x-ray lines; CR calculations CRETIN [23], and SCRAM [22] indicated abundant He-like ion fractions at these densities and temperatures (2–5 keV); and krypton, which is a noble gas, can be easily added to the D gas in precise concentrations. The calculated optical depth from SCRAM for a 50 μm capsule thickness at an electron density of 5×10^{24} cm^{-3} is approximately 0.45 for Kr Heβ and ~8 for Kr Heα. A platform was developed for Kr-doped DD capsules, [38, 39] and NIF experiments were performed using a somewhat lower resolution NIF x-ray spectrometer [40] to assess the performance of these earlier experiments. Experiments were performed with Kr concentration levels of 0.01, 0.02, and 0.03 atomic percent and were compared with detailed simulations in order to assess the optimal concentration to provide sufficient x-ray signal while maintaining acceptable degradation of fusion yield due to radiative cooling and increased hydrodynamic instability.

To facilitate the interpolation of the four Stark profiles shown in figure 1 to intermediate densities, each profile was approximated by a best fit to the sum of three Voigt functions. Although the situation is more complicated in that a total of ten 1s3l upper levels form the basis functions for the x-ray transitions, the spectra in figure 1 appear to be mainly dominated by three peaks. Voigt functions were selected because they can represent the natural radiative decay spectrum, which is a Lorentzian, convolved with other non-Lorentzian shapes that might be represented by Gaussian profiles, such as spectrometer resolution functions and Doppler broadening. An example of the multiple Voigt 'fitting' is shown in figure 2 for the Kr Heβ Stark broadened profile at $T_e = T_{ion} = 3$ keV and $n_e = 5 \times 10^{24}$ cm^{-3}. The upper solid black curve is the original theoretical line shape, the lower solid black, red, and blue curves are the three individual Voigt functions, and the dashed red curve is the approximation to the theoretical line shape, or the sum of the three Voigt functions. For comparison, the positions of the three multiplets of the unperturbed

He-like (1s 3p) configuration, as well as the centroid of Li-like satellites (magenta, dashed) near the He-like 3 $^3P_1$ unperturbed multiplet are shown as vertical dashed lines. These He-like multiplets are specifically the (1s 3p) singlet P resonance line, 3 $^1P_1$, the triplet p, or 3 $^3P_1$, and the $n = 3$ singlet D, 3 $^1D_2$ states. These three energies of the unperturbed states are indicated, and they are the positions to which the centroids of the three Voigt fitting functions approximately extrapolate at zero electron density.

One can see that the Voigt sum (red dashed curve) approximates the original theoretical Stark profile (top solid black) very well except at the lowest energies. The small deviations on the low energy wing near 15.39 keV are inconsequential for the present study because only the two higher energy peaks (sum of the red and blue Voigt profiles) were used for the analysis of the composite Heβ lineshape. These deviations simply mean that additional spectral components would be required to fully approximate the profiles produced by the SimU code. To simplify future discussions, the three peaks are labeled 1 for the central peak and 2 for the high energy peak, and 0 for the low energy peak, which is not included in the linewidth analyses.

From these approximate decompositions of the line shapes of figure 1, the variation of the Voigt parameters with electron density, as shown in figure 3, can be obtained. The electric microfield strengths have some proportionality with the electron density; therefore, the dependencies shown in figure 3 indicate how the various Stark-broadening and shifting effects depend on the microfields.

With the parameterizations of the Voigt parameters, as shown in figure 3, approximations to the simulated Stark-broadened profiles can be interpolated to electron densities between 1×10^{24} cm^{-3} and 10×10^{24} cm^{-3}. The interpolation is done by a quadratic fit to the four given density points (densities of 1, 3, 5, and 10 in units of 10^{24} cm^{-3}), which is shown as the solid curves in figure 3. Because the densities of the NIF hot spots inferred from dHIRES were in the range of 1.8–4.0 $\times$ 10^{24} cm^{-3}, it is reasonable to suspect that the densities interpolated from theoretical values of 1.0, 3.0, and 5.0 $\times$ 10^{24} cm^{-3} might have reasonably small errors.

A theoretical interpretation of the dependencies on density shown by the curves in figure 3 can be described as follows: the energy splitting shown in figure 3(a) results from an energy shift, mainly of the upper level, as a result of the usual (dipole) Stark effect—mixing of states with different parity by the electric field due to the perturbing background electrons and ions. Shifts due to other phenomena - continuum lowering and plasma polarization shift - are not included. The variation in relative peak intensities with electron density in figure 3(b) can be interpreted as a variation in the mixing of the basis levels due to the perturbation by the electrical microfields. The broadening of the individual peaks with increasing density shown in figure 3(c) is predominately due to the ion microfield distribution: the ion dynamics (the 'ion dynamic' effect) contributes to the overall line shape. A smaller contribution to the broadening is an additional density-dependent reduction in the lifetime of the excited state ($\Delta E \Delta t = h/2\pi$) owing to electron-impact collisions. For the theoretical Stark profile to match the experimental profile shape, each of these dependencies (shift, relative intensity, and broadening) should be properly calculated simultaneously. The matching of theory and experiment also depends on an accurate measurement of the spectral shape.

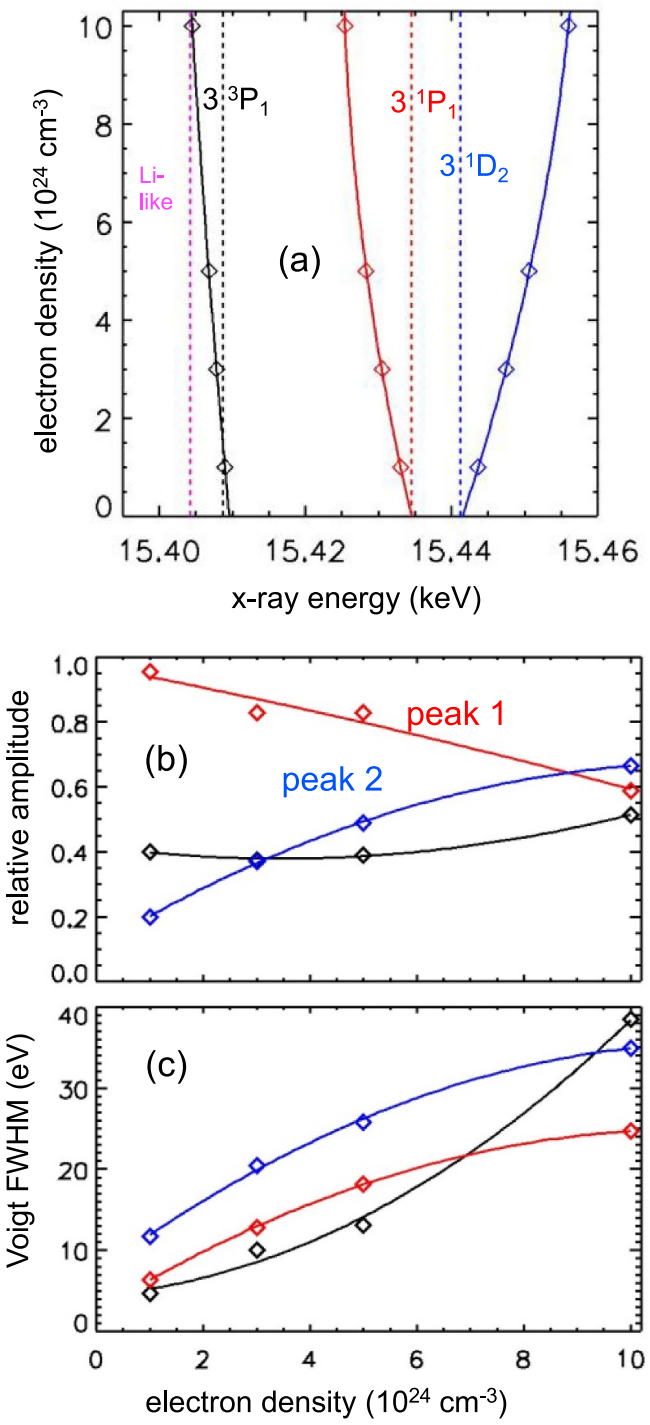

Figure 3. Variation of Voigt parameters (a) center positions, (b) relative amplitudes, and (c) widths (FWHM—full width at half maximum), with electron density. The diamonds are graphed at $n_e = 1\times, 3\times, 5\times$ and 10×10^{24} cm^{-3} in all sub-figures. $T_e = 3$ keV for all cases. Vertical dashed lines in (a) represent energies of the three unshifted He-like lines and the centroid of unshifted Li-like dielectronic satellites to the He-like resonance line 3 $^1P_1$.

3. Results

3.1. Experimental dHIRES Kr He β spectra and comparison with theory

The dHIRES spectrometer can measure absolute Kr Heα and Heβ spectra in units of, for example, J keV^{-1} sr^{-1} s^{-2}. The dHIRES instrument comprises three different x-ray spectrometers in one chamber [14, 15]. Two of the spectrometers sagittally or spatially focus their spectra on different parts of the photocathode of a fast x-ray streak camera and, thus, provide time-resolved spectra. One spectrometer covers the Kr Heα and Lyα range (12.8–13.6 keV) and the other covers the Kr Heβ range of energies (14.9–15.6 keV). Since the photocathode is perpendicular to a line from source to photocathode, a special crystal geometry, the Hall conical crystal configuration, [41, 42] is used for these two time resolving spectrometers. The third spectrometer is a time-integrated von Hamos spectrometer [43] that covers the full Heα and Heβ energy ranges and all energies between these ranges ($\sim$12.8–15.6 keV), recording the spectra on an IP. Because the IPs have been absolutely calibrated, and the throughputs of all three dHIRES spectrometers have been measured, the absolute calibration of the time-integrated spectrum can be transferred to the time-resolved spectra. Thus, dHIRES provides spectra in absolute units of J keV^{-1} sr^{-1} s^{-1}. Although the measured spectra can be displayed in absolute physical units, this capability is not used in this study because the measurements of n_e and T_e presented here rely only on the peak widths or ratios of intensities of two peaks, neither of which depends on the absolute amplitude of the Heβ spectral peaks.

In this paper we are focusing on only the Heβ spectrum and its application to measuring the electron density (n_e) and electron temperature (T_e) of the 'hot spot' of the compressed capsules. A sample spectrum covering both the Kr Heβ complex at 15.43 keV and a Li-like peak near 15.29 keV is shown in figure 4(a). In figure 4(b) the Kr Heβ peak is expanded for better visual comparison of the four overlaid spectra. The measured spectrum is represented by the dashed black curve. The additional curves are the simulated Stark broadening curves interpolated from the theoretical model, SimU, shown in figure 1 (red); a simulation from the SCRAM [22] collisional radiative code (blue); and a simulation from the CRETIN [23] collisional radiative code (green). The theoretical Stark profiles were convolved with a 12 eV wide full width at half maximum (FWHM) Gaussian function to account for the instrumental resolution of the spectrometer plus a Doppler broadening component of approximately 7 eV for Kr at $T_{ion} = 3$ keV.

In figure 4 the red curve was calculated for an electron density of 3.9×10^{24} cm^{-3}, which provided a close fit to the measured profile shape. The electron density was inferred from Stark broadening of the Heβ resonance line complex near 15.43 keV, and the electron temperature was inferred from a comparison of the ratio of intensity of the peak near 15.29 keV to the intensity of the 15.43 keV peak to the intensity ratios of SCRAM simulated spectra (figure 7). For simplicity in the following discussion the central peak near 15.42–15.43 keV will be referred to as peak 1, and the higher energy peak near 15.44–15.45 keV will be referred to as peak 2.

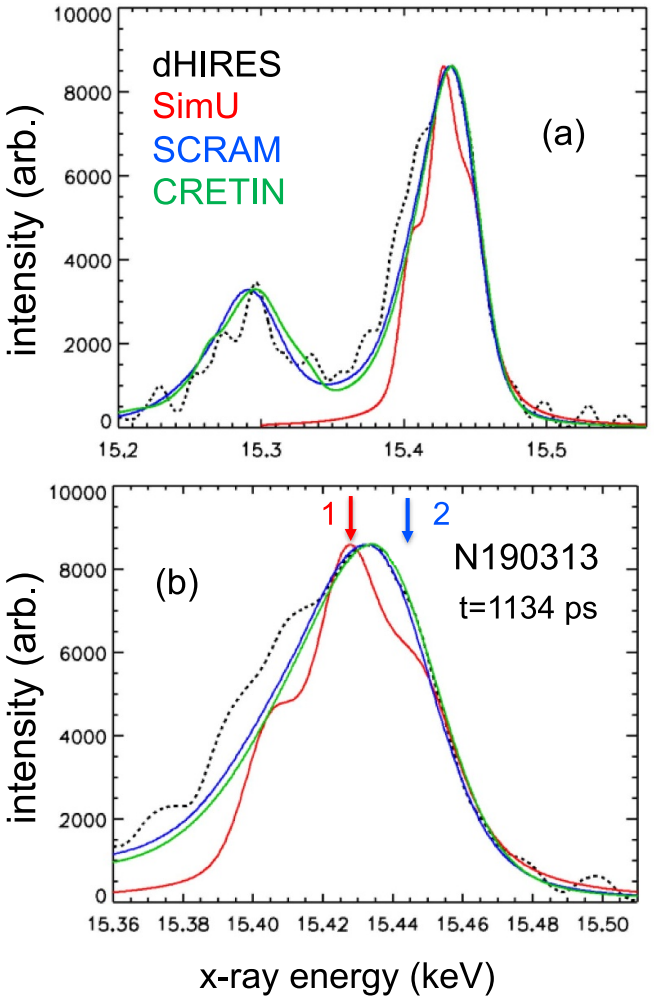

Figure 4. (a) Li-like and He-like Kr features, and (b) only the Kr Heβ peak. Different curves explained in the text. The red and blue arrows are to guide the eye to the approximate locations of the two Voigt components, 1 and 2 as labeled in figure 3. The inferred electron density is 3.89×10^{24} cm^{-3}, as listed at time 1134 ps in figure 5.

A robustly observed discrepancy between the measured and theoretical line profile shapes is shown in figure 4(b). In the red theoretical curve, the distinction between the higher energy peak, peak 2, and the central energy peak, peak 1, is evident; however, a similar separation is either non-existent or much less evident in the dashed measured curve. This difference between the theoretical and experimental peaks exists even though the theoretical peak has been convolved with a 12 eV FWHM Gaussian function to approximate the instrumental function of the spectrometer plus Doppler broadening. It appears that the intensity of peak 2 relative to peak 1 is too low. It is not clear what the cause of this discrepancy is; simply increasing the width of the spectrometer Gaussian function from 12 eV to 15 eV makes little difference. One thought is uncorrected opacity broadening which might be more predominant in flattening peak 1 than for peak 2.

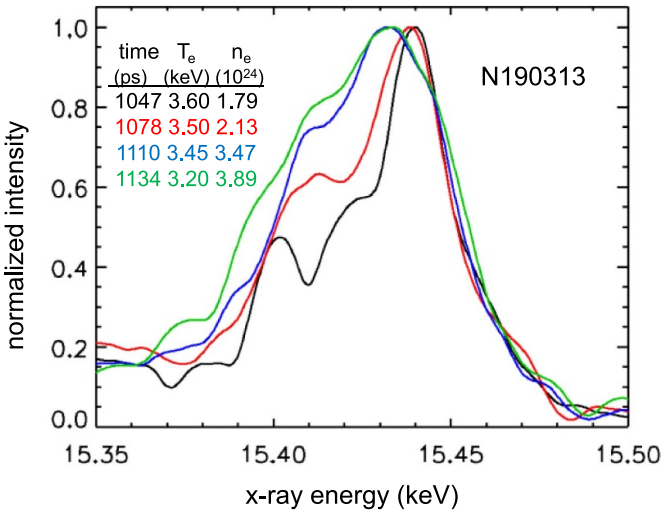

Figure 5. Measured Kr Heb spectrum for shot N190313 at four times showing the broadening and shift of the line centroid to lower energy with increasing time. Also shown are the inferred values of T_e and n_e at those times.

The width of the simulated composite peak (i.e. peak 1 plus peak 2) in figure 4, red curve, can be made to match the width of the measured curve by slightly modifying the parametric dependences on electron density of the Stark splitting, relative amplitude of peaks 1 and 2, and Voigt width as shown in figures 3(a)–(c), respectively. That is by evaluating the relative peak intensities at a density 20% higher than nominal density (3.89×10^{24} cm^{-3}) in figure 4, while evaluating the splitting and Voigt widths at a density 20% lower than the nominal density. This type of study, however, in which one varies the strength of the effect of the electric field on the various physical processes should be performed at the theoretical level, because it is not known at the experimental level which of the physical dependencies might have larger calculational uncertainties.

An example of a shot in which the width of the Kr Heβ resonance line feature increases significantly with time is shown in figure 5. It can be clearly seen in this figure that the relatively narrow feature near 15.44 keV in the black trace at time 1047 ps broadens later in time (1078 ps) in the red profile, and further broadens and shifts to lower energy at later times in the blue (1110 ps) and green (1134 ps) curves. In addition, the higher energy side of the peak at an intensity of 0.5–0.6 is seen to shift slightly to higher energies with increasing time. This broadening and shift of the Kr Heβ complex over time is attributed to Stark broadening due to increasing electron density, and the broadening enables an inference of the electron density (see figure 1) by comparison of the width with the theoretical simulations of the code SimU. It is further seen that the centroid of the spectral peak shifts to lower energy with increasing time, which can provide a check or comparison to theories of energy level shifts at high density.

Note that the curves in figure 5 are measured spectra, and the absolute energy scale has significant uncertainties, possibly several eV. This uncertainty derives from possible pointing and position errors of the dHIRES spectrometer relative to the emitting target. The specified uncertainty in the DIM's ability to position the instrument laterally is $\pm$0.5 mm, which in the spectrometer dispersion plane, translates to a possible energy scale uncertainty of $\pm$28 eV (see figure 9, right panel, top figure of [15]). Thus, the energy scale was obtained by assigning theoretical energies to the two main peaks, Li-like and He-like Kr, of the time integrated spectrum, in order to obtain the best statistics, and these energies are not well known because of density dependent redshifts of the spectral lines [44–47].

The widths of spectral lines are normally quantified by the FWHM. However, it is known that Li-like spectral lines of unknown intensity lie near the lower-energy features in the vicinity of 15.42 keV. Therefore, in order to minimize the additional broadening from this Li-like line contamination, we quantified the width by an asymmetric measurement from near the peak on the lower energy side (say 90% of peak value) to 30%–50% of peak height on the high energy side. We call these positions lower (at lower energy) and upper 'thresholds', taking the term from energy dispersive, or pulse-height, spectroscopy. We then compared this measured line width with the width of the theoretical Stark broadened line shapes from SimU (figure 1) between the same thresholds, or fractions of the peak maximum, and selected as the inferred electron density when the theoretical width matched the experimental width. In order to account for the shape of the high energy wing of the peak, we perform this 'fitting' for multiple upper thresholds and take the inferred electron density as the average of these multiple values. Furthermore, we estimated the effect of the Li-like Kr line by comparing the similarly obtained widths of SCRAM simulations of a Li- plus He-like Kr spectral simulation versus a He-like only simulation and found that the correction is typically of the order of 10%–15% in the relevant density range of 2×10^{24}–5×10^{24} cm^{-3}. The electron densities shown in figures 8–11 were corrected for this additional broadening factor.

The basis for determining electron temperature is shown in figure 6. These are Kr Heβ spectra calculated by SCRAM at a density of 3×10^{24} cm^{-3} and for electron temperatures ranging from 2.5 to 6.0 keV. The spectra were all normalized to the same value at the peak of the Kr Heβ resonance line near 15.425 keV. The lower energy peak near 15.28 keV contains a Li-like Kr feature whose intensity has a significant contribution owing to dielectronic recombination. This variation in the relative intensities of the two peaks results from the fact that the rate of dielectronic excitation decreases with electron temperature, whereas the rate of impact excitation of the 15.43 keV line increases with temperature [48]. Thus, we can infer the electron temperature from the measured spectrum in figure 4 by choosing the temperature and density at which the relative intensities of these two measured peaks match those of the SCRAM or CRETIN spectra.

The time histories of the asymmetric width of the Kr Heβ resonance line complex from lower energy thresholds near 0.9 to higher energy thresholds near 0.40 for the four different shots are shown in figure 7.

The data in figure 7 were plotted for the times during which the Kr Heβ spectrum was sufficiently intense to

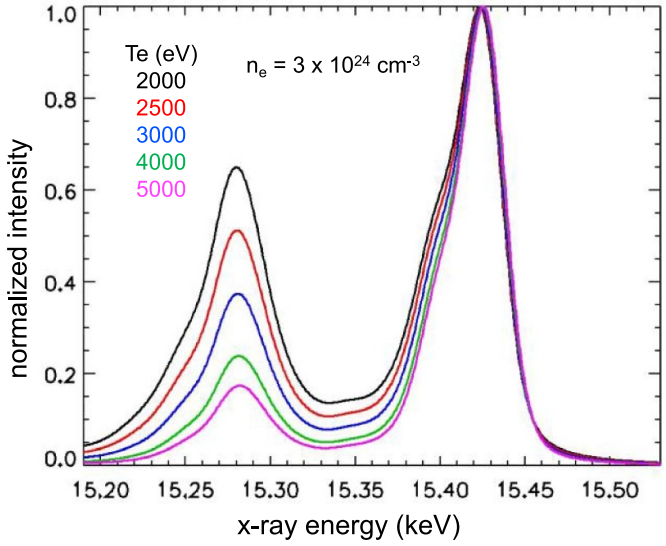

Figure 6. Normalized Kr Heβ spectra simulated by SCRAM for an electron density of 3×10^{24} cm^{-3} and electron temperatures ranging from 2000 eV to 5000 eV. The intensity ratio of the lower energy peak to the higher energy peak is compared with the same ratio of the measured spectra to infer the measured T_e.

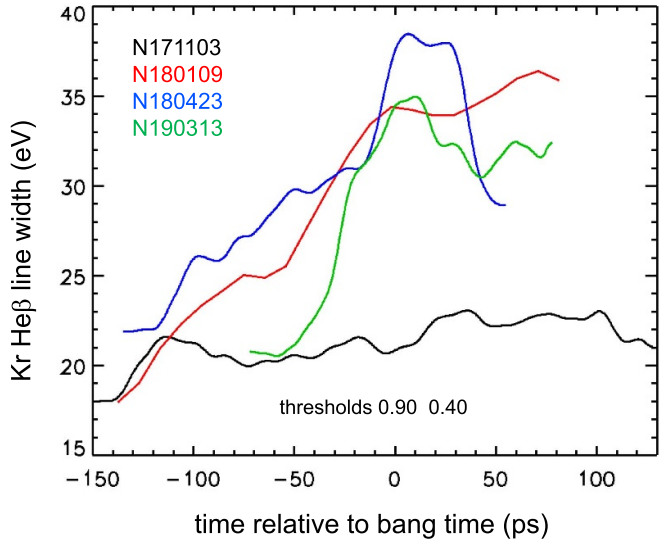

Figure 7. Time histories of Kr Heβ peak widths, relative to time of Kr Heβ x-ray maximum intensity (x-ray 'bang time'), as measured asymmetrically between the indicated thresholds of 90% of peak line intensity on the left side to 40% on the right side, for four different NIF shots. Note that the spectral width for shot N171103 remains significantly narrower than that of the other shots, indicating a lower electron density.

allow statistically a meaningful analysis. Shot N171103 was a 'Bigfoot' [49] shot with an undoped CH shell, and shot N180109 was a tungsten doped bigfoot shot with CH shell. Shot N180423 was a 'Pushered Single Shell' (PSS) [50, 51] shot with a Si doped CH shell, and N190313 was also a PSS shot, but with both Si and Cu dopants in the shell.

From measured Kr Heβ widths such as those shown in figure 7 and the theoretical increase in line width with increasing density, as shown in figure 1, we can infer the time

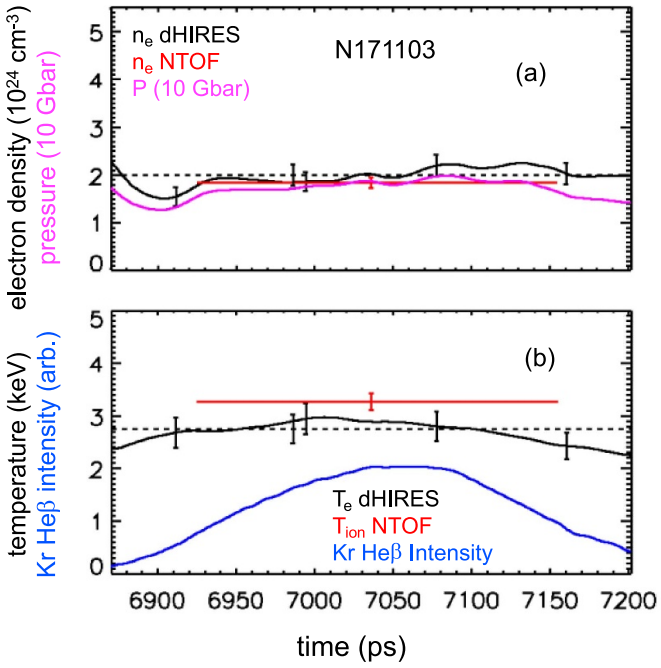

Figure 8. (a) Electron densities from dHIRES and NTOF and plasma pressure from dHIRES, (b) electron temperature and Kr line intensity from dHIRES overlaid with T_{ion} from NTOF. See text for detailed explanation. The 'bang' time (time of maximum neutron emission) is 7040 ps, and the burn width is 230 ps.

evolution of the electron density, which is plotted as a solid black curve in figure 8(a) for shot N171103, and for other shots in figures 9–11. It should be noted, however, that the plots in figure 7 are shown more for relative comparisons of the measured widths for the different shots, and should be considered as less quantitative than the inferred electron densities graphed in figures 8(a)–11(a) for two reasons. First the data in figure 7 involve a width for a single upper or high energy threshold of 0.4, whereas the densities in the later figures are inferred for three different upper thresholds, typically 0.4, 0.5, and 0.6, in order to better match the shape of the upper wing of the data to the detailed shape of the theoretical curve. The final density is taken as the average of the three individual densities. Secondly, to avoid overly restricting the time variation of the widths in figure 7, a final smoothing time of 15 pixels, or about 7 ps is applied, whereas a longer smoothing time of 50 pixels is applied for figures 8–11 to more closely match the nominal time resolution of the x-ray streak camera of 25–30 ps.

In addition, by comparing the measured ratio of the intensities of the Li-like Kr peak to the He-like peak ('Li/He' ratio) with SCRAM and CRETIN simulations we obtain the electron temperature time history as the solid black curve in figure 8(b), which is the average of the T_e values derived from SCRAM and CRETIN. The difference between these two values is small and is displayed as a component of the error bars in figure 8(b).

The dashed black curve in figure 8(a) is the Kr Heβ intensity weighted time average of the solid black curve, and the solid red line is the electron density estimate inferred from the secondary deuteron-triton (DT) neutron analysis of the

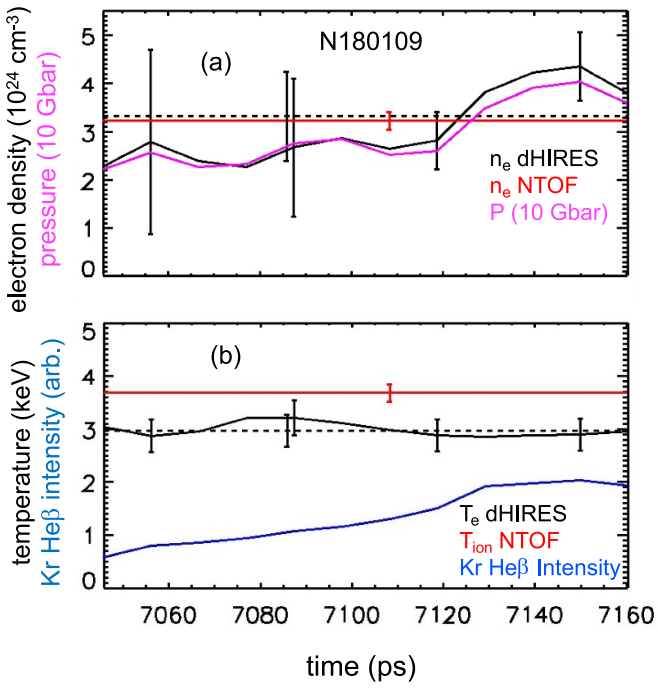

Figure 9. Same parameters, n_e, T, and pressure, for shot N180109 as described in figure 8 and in the text. Fusion bang time and burn width not available for this shot.

neutron time-of-flight (NTOF) diagnostic [5, 6]. Both of these flat curves represent single point values and are graphed as horizontal lines according to the time over which they were integrated. Note that the red line does not cover the full time of the abscissa; it is shortened to indicate that it covers or is relevant only over the fusion 'burn' time or the time of neutron emission. The magenta curve represents the total pressure in units of 10 GBar, assuming equal electron and ion temperature. In figure 8(b) the solid black curve is the average of the two T_e values derived from SCRAM and CRETIN and is taken as the measured T_e. The solid blue curve represents the measured Kr Heβ peak intensity. The black dashed curve is the Kr intensity weighted time average of the solid black curve, and the red solid line is the T_{ion} inferred from the NTOF diagnostic.

The solid black curve in figure 8(a) is the average electron density from the three asymmetric widths spanning from a threshold of 0.9 (times Kr Heβ peak height) on the left side of the Heβ peak to thresholds of 0.3, 0.4, and 0.5 on the right side. The solid red curve is the electron temperature inferred from the Li/He ratio of the intensities, compared with the SCRAM simulations. The solid red line is the electron density estimate inferred from the secondary DT neutron analysis of the NTOF diagnosis. Note that the electron density varies from about 1.7 to 2.3 in units of 10^{24} cm^{-3} for this shot, while electron temperature ranges from about 2.5 to 3.0 keV. The maximum pressure in this undoped bigfoot shot is approximately 20 Gbar.

In figure 8(b) the solid black curve is the average of the two T_e values derived from SCRAM and CRETIN, which was taken as the measured T_e. The solid blue curve represents the measured Kr Heβ line intensity. The black dashed curve is the Kr intensity-weighted time average of the solid black curve, and the red solid line is the T_{ion} inferred from the NTOF diagnostic.

The time evolution of these same parameters for shot N180109 is shown in figure 9. We see that the electron density is much higher for this shot, which has a tungsten dopant in the shell, ranging from 2.3 to 4.3 in units of 10^{24} cm^{-3}, while the electron temperature is in the range of 3.0–3.3 keV. For comparison, the electron temperature inferred from the 20 to 30 keV x-ray continuum as measured by ConSpec [12, 13] was 3.65 keV with error bounds of 3.42–3.98 keV. In addition, the maximum pressure is approximately 40 Gbar, which is twice that of the undoped bigfoot shot of figure 8(a), as reported previously by Gao *et al* [2].

Although the present study deals with capsules filled with D only, this improved pressure is consistent with and further supports the use of high-Z dopants to improve performance, also, in DT shots. Berzak Hopkins *et al* [52] reported a 40% increase in hot spot pressure and a 55% increase in neutron yield from W-doped capsules in DT experiments versus undoped capsules.

The large error bars for density in figure 9(a), result from the fact that the noise level of the x-ray streak camera is very high, as explained in section 4.2, uncertainty analysis, and for shot N180109 the signal or count rate level was low due to excessive titanium-foil filtration. The over-filtration of this shot resulted as an overreaction to the fact that the signal levels in the previous shot from figure 8 were high and were thought to be approaching levels at which the streak-tube imaging resolution could be broadened due to space-charge effects.

The time evolutions of these same parameters for shots N180423 and N190313 are shown in figures 10 and 11, respectively.

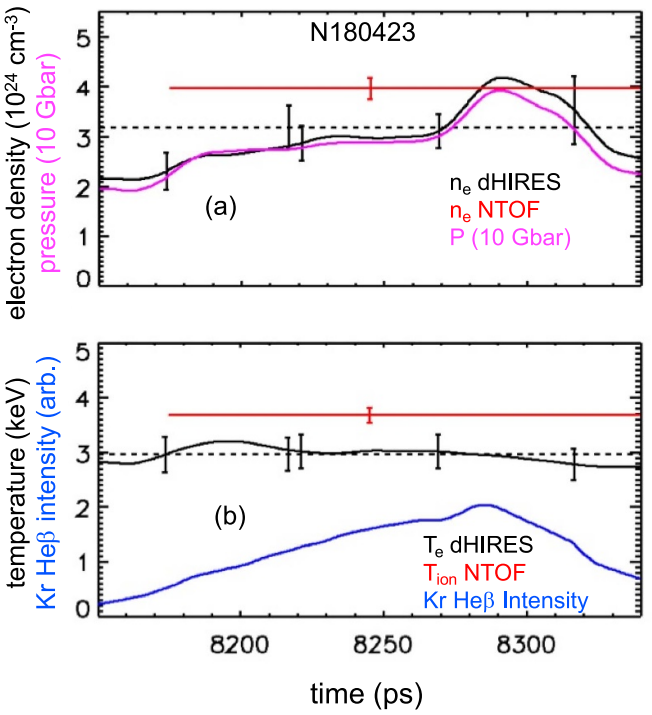

Figure 10. Same parameters, n_e, T, and pressure, for shot N180423 as described in figure 8 and in the text. Fusion bang time and burn widths are 8260 and 170 ps, respectively.

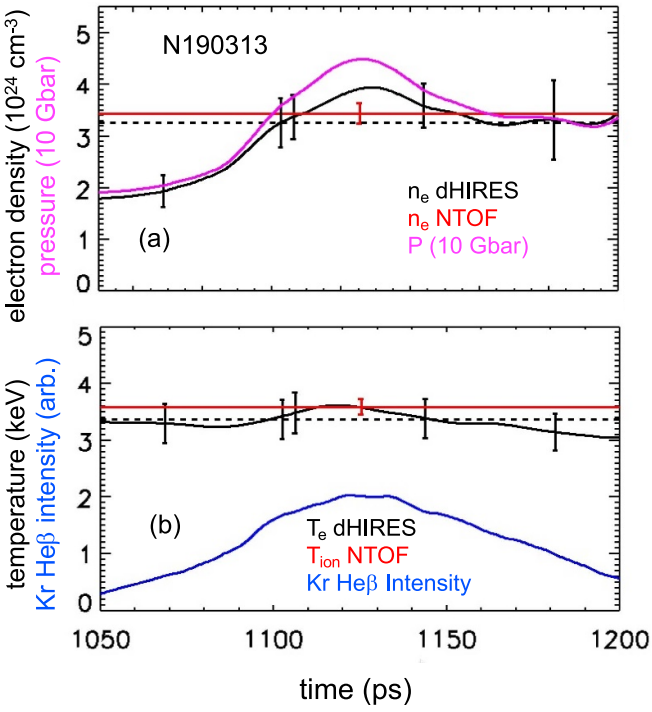

Figure 11. Same parameters, n_e, T, and pressure, for shot N190313 as described in figure 8 and in the text. Bang time and burn widths about 1123 and 160 ps, respectively.

3.2. Kr Heb line shifts

In high-density plasmas the bound electrons in ions experience fields owing to the surrounding particles that perturb their energy levels, leading to line shifts, line broadening, and continuum lowering [53]. Understanding these effects theoretically are important for, for example, using line widths or shifts to measure density, detailed prediction of the dense plasma equation of state and radiative opacity in stellar interiors, ICF research, and planetary interiors [54]. Until recently, discrepancies had been observed between the measurements and existing theories for continuum lowering and line shifts [44, 53]. More recent studies have apparently removed most of these discrepancies [47, 55]. The measured redshifts of the Kr Heβ peak, as observed in figure 5 and as quantified by the centroid of the peak taken from thresholds of 90% of peak height on both the left and the right sides of the peak, range from about 6 eV to 12 eV, and increase with inferred densities in the range 1.8–4.0 $\times$ 10^{24} cm^{-3}. A discussion of these measurements and comparisons with the theory of Li and Rosmej [44, 47], and other theories if available, is beyond the scope of this paper and will be presented in a future publication.

4. Discussion

4.1. Summary of measurements and comparison with measurements from neutron diagnostics

The Kr Heβ intensity weighted, time averaged electron densities and temperatures measured by dHIRES for the four different NIF shots are summarized in table 1 and compared with electron densities and ion temperatures measured by the NTOF diagnostic [6]. The values in parentheses represent the uncertainties (standard deviation) in the cited values for density and temperature. One sees that the dHIRES and NTOF densities agree within error bars for all but shot N180423, in which the NTOF density is considerably higher than the value from dHIRES. In addition, note that for all shots, the NTOF value of the ion temperature was significantly higher than the electron temperature inferred from dHIRES. The differences range from 520 to 710 eV for the two bigfoot shots, and 710 and 220 eV for the two PSS shots.

The fact that the NTOF measured values of $T_{\rm ion}$ are higher than the dHIRES values of $T_{\rm e}$ is not surprising since the apparent ion temperature values, $T_{\rm ion}$, as measured by NTOF, were observed to be higher than those expected from simulations and to be in disagreement with the observed neutron yields [7]. For example, Chrien *et al* [56] reported that NTOF measured $T_{\rm ion}$ values ranging from 1.94 to 2.55 keV, depending on the level of Ge dopant, while the fusion-burn-weighted ion temperatures predicted by the LASNEX [57] two-dimensional radiation hydrodynamics code was 1.7 keV. In another example, simulated $T_{\rm ion}$ was 550–600 eV, while the value inferred from neutrons was 1.43 $\pm$ 0.17 keV. In this case, while the measured and simulated neutron yields were similar, predictions of neutron yields using the higher, measured $T_{\rm ion}$, which results in a 200 times higher fusion reactivity, would be difficult to reconcile.

The $T_{\rm e}$ values from dHIRES are expected to be very close to the thermal ion temperature values since the electron-ion relaxation time for a deuterium plasma with an electron temperature of 3 keV and electron density of 2 $\times$ 10^{24} cm^{-3} is

Table 1. Summary of time averaged electron densities and temperatures measured by the dHIRES diagnostic for the four performance qualification (PQ) shots, and comparison with electron density and ion temperature measured by the NTOF diagnostic. The values in parentheses represent the uncertainty (standard deviation) in the cited values.

Platform/hohlraum	Shot ID	Dopant	n_e time avg. 10^{24} cm^{-3}	n_e NTOF 10^{24} cm^{-3}	n_e difference 10^{24} cm^{-3}	T_e time avg. keV	T_{ion} NTOF keV	T difference keV
Bigfoot Au PQ1	N171102	None	2.00 (0.074)	1.84 (0.11)	−0.16	2.75 (0.026)	3.27 (0.16)	0.52
Bigfoot Au PQ2	N180109	W	3.34 (0.44)	3.23 (0.18)	−0.11	2.97 (0.025)	3.68 (0.16)	0.71
PSS Au PQ3	N180423	None	3.19 (0.277)	3.97 (0.21)	0.78	2.97 (0.052)	3.68 (0.14)	0.71
PSS Au PQ4	N190313	Cu	3.26 (0.418)	3.44 (0.20)	0.18	3.37 (0.055)	3.59 (0.14)	0.22

calculated [58] to be about 7 ps, and the temporal resolution and smoothing of the dHIRES measurements is about 30 ps. Murphy [7] explains that in a plasma with a Maxwellian distribution of ion energies, the spread of neutron energy arises from the thermal spread in the center-of-mass velocities of the reacting pairs of ions. Fluid velocities in ICF are of a similar magnitude as the center-of-mass velocities and can lead to further broadening of the neutron spectrum, leading to erroneous inference of the ion temperature. From the additional broadening Murphy [7] showed that the fluid motion velocity can be calculated, but the application of this theory to the present enhancements of NTOF T_{ion} above dHIRES T_e is beyond the scope of this work.

4.2. Uncertainty analysis

The uncertainties or error bars in figures 8–11 were derived via a Monte Carlo technique from the pixel-to-pixel count fluctuations in the signals from the charge-coupled device (CCD) detector that recorded the streaked spectra processed by the x-ray streak tube [59]. This approach can account for several processes that can add to the uncertainty in the measurements. Briefly, these processes are the photon counting event statistics, single pixel spikes due to either DD neutrons or hard x-rays that penetrate the shielding and reach the CCD, and fluctuations in the signal due to several internal conversion processes inside the streak camera. The neutron spikes are mostly removed by 2D median filtering, but residual 'stubble' remains and adds to the 'noise.' The internal conversions in the streak camera are x-ray to photoelectrons at the photocathode with a distribution in number and energy; conversion of accelerated and streaked photoelectrons to secondary electrons at the input of the microchannel plate (MCP) imaging electron multiplier, which electrons have a distribution in number and energy; variation of gains and output electron number distributions at the exit of the MCP pores; statistical variations in the number of visible photons produced by the accelerated MCP output electrons on a phosphor screen; losses in coupling the visible photons to the CCD; and statistical variations in the conversion of these photons to electron–hole pairs in the CCD.

Typically, 5000 Monte Carlo variations in the spectra and spectral energy points were calculated, and the electron density and temperature were deduced from these spectra, thus providing variations in the density and temperature inference from which the standard deviations in n_e and T_e were deduced. The Kr Heβ x-ray spectra were streaked in time by the DISC [59] (DIm Streak Camera, where DIM stands for Diagnostic Instrument Manipulator). The streaked images were ultimately recorded on a ∼2000 × ∼600 pixel section of a 4k × 4k CCD with spectra dispersed in the x-direction and time in the y-direction. Since the time resolution of the DISC streak camera is about 25–30 ps, the spectral images have been smoothed by about 60 pixels in the y (temporal) direction, corresponding to about 25 ps in time duration.

To estimate the fluctuation statistics in each pixel column, the mean and standard deviations were calculated in a ∼60 pixel sliding window (temporal direction) for each column, thus providing the fluctuation standard deviation at each pixel. These fluctuation standard deviations are the ones used to specify Monte Carlo variations of spectral intensity at each pixel, thus enabling the estimates of uncertainty in n_e and T_e.

4.3. Conclusions

A modestly high resolution x-ray spectrometer, called dHIRES, has been installed on the NIF and has been used to measure, using Kr Heβ spectra, the temporal evolution of T_e, n_e, and the redshifts of the Heβ resonance line during the stagnated phase of NIF capsule implosions. The temperature and pressure in an ignition capsule near the stagnation time indicate the quality of the implosion. Therefore, accurate time resolved measurements of the hot-spot plasma parameters are important for assessing the implosion performance toward understanding how to achieve ignition. Most current techniques for measuring hot spot temperature and density are time-integrated and, therefore, do not elucidate the time evolution of the hot spot parameters during the stagnation phase.

These parameters were measured for four NIF shots, and the time-averaged values of the measured n_e and T_e were compared with the measurements from neutron diagnostics. The dHIRES n_e values agree within uncertainties with neutron based measurements for three of the four shots; The dHIRES T_e values are 200–700 eV lower than the T_{ion} measurements from the NTOF diagnostics; this difference is consistent with previous observations that the T_{ion} value derived from NTOF can be higher than the real ion temperature due to enhancement of the neutron spectral width by plasma flows. This new capability of measuring the time history of the basic plasma parameters during the stagnation phase of capsule compression should enable benchmarking of code simulations to improve

understanding of the physics of this important phase and help advance the quest for ICF ignition.

In addition, the time evolutions of the redshifts of the central Heβ line were measured and exhibited maximum values of 5–12 eV. A future study is planned to present a more detailed analysis of these redshifts and a comparison with theoretical calculations.

Data availability statement

The data that support the findings of this study are openly available at the following URL/DOI: https://arks.princeton.edu/ark:/88435/dsp01x920g025r.

Acknowledgments

This work was performed under the auspices of the US Department of Energy by the Princeton Plasma Physics Laboratory under Contract DE-AC02-09CH11466, by Lawrence Livermore National Laboratory under Contract DE-AC52-07NA27344, and by the Weizmann Institute of Science with support of DOE/NNSA via NRL.

Conflict of interest

The authors have determined that no competing interests exist.

ORCID iDs

K W Hill https://orcid.org/0000-0002-2494-8125
B F Kraus https://orcid.org/0000-0002-5713-9316
N Pablant https://orcid.org/0000-0001-6617-8459
M J MacDonald https://orcid.org/0000-0002-6295-6978
E Stambulchik https://orcid.org/0000-0002-7100-8793

References

[1] Lindl J 1995 *Phys. Plasmas* **2** 3933
[2] Gao L *et al* 2022 *Phys. Rev. Lett.* **128** 185002
[3] Betti R, Umansky M, Lobatchev V, Goncharov V N and McCrory R L 2001 *Phys. Plasmas* **8** 5257
[4] Hurricane O A *et al* 2019 *Plasma Phys. Control. Fusion* **61** 014033
[5] Grim G P *et al* 2013 *Phys. Plasmas* **20** 056320
[6] Rinderknect H G *et al* 2015 *Phys. Plasmas* **22** 082709
[7] Murphy T J 2014 *Phys. Plasmas* **21** 072701
[8] Gatu Johnson M *et al* 2016 *Phys. Rev.* E **94** 021202
[9] Hill K W *et al* 2016 *26th IAEA Fusion Energy Conf.* (*Kyoto, Japan*) IFE/P5-6
[10] Jarrott L C *et al* 2018 *Phys. Rev. Lett.* **121** 085001
[11] Jarrott L C *et al* 2016 *Rev. Sci. Instrum.* **87** 11E534
[12] Thorn D B *et al* 2017 *Proc. SPIE* **10390** 1039009
[13] MacDonald M J, Kozioziemski B, MacPhee A G, Schneider M B, Ayers J and Thorn D B 2019 *J. Instrum.* **14** P12009
[14] Hill K W *et al* 2016 *Rev. Sci. Instrum.* **87** 11E344
[15] Gao L *et al* 2018 *Rev. Sci. Instrum.* **89** 10F125
[16] Stark J 1914 *Ann. Phys.* **43** 965
[17] Griem H R 1964 *Plasma Spectroscopy* (New York: McGraw-Hill)
[18] Baranger M 1962 *Atomic and Molecular Processes* ed D R Bates (New York: Academic) ch 13
[19] Cooper J 1967 *Rev. Mod. Phys.* **39** 167
[20] Rosmej F B, Deschaud B, Bennadji K, Indelicato P and Marques J P 2013 *Phys. Rev.* A **87** 022515
[21] Stambulchik E and Maron Y 2006 *J. Quant. Spectrosc. Radiat. Transfer* **99** 730
[22] Hansen S, Bauche J, Bauche-Arnoult C and Gu M 2007 *High Energy Density Phys.* **3** 109
[23] Scott H A 2001 *J. Quant. Spectrosc. Radiat. Transfer* **71** 689
[24] Goryaev F F, Vainshtein L A and Urnov A M 2017 *At. Data Nucl. Data Tables* **113** 117
[25] (Available at: www.nist.gov/pml/atomic-spectra-database)
[26] (Available at: https://github.com/fnevgeny/cfac)
[27] Gu M F 2008 *Can. J. Phys.* **86** 675
[28] Woltz L A, Iglesias C A and Hooper C F Jr 1982 *J. Quant. Spectrosc. Radiat. Transfer* **27** 233
[29] Woolsey N C *et al* 1996 *Phys. Rev.* E **53** 6396
[30] Woolsey N C *et al* 1997 *J. Quant. Spectrosc. Radiat. Transfer* **58** 915
[31] Gigosos M A 2014 *J. Phys. D: Appl. Phys.* **47** 343001
[32] Inglis D R and Teller E 1939 *Astrophys. J.* **90** 439
[33] Stewart J C and Pyatt K D Jr 1966 *Astrophys. J.* **144** 1203
[34] Massacrier G and Dubau J 1990 *J. Phys.* B **23** 2459S
[35] More R M Atomic physics in inertial confinement fusion *LLNL Technical Report No. UCRL-84991* (unpublished)
[36] Chung H-K, Chen M H, Morgan W L, Ralchenko Y and Lee R W 2005 *High Energy Density Phys.* **1** 3
[37] Cho M S, Matsuo K, Fujioka S, Hahn S J, Cho B I and Chung H K 2020 *J. Quant. Spectrosc. Radiat. Transfer* **257** 107369
[38] Ma T *et al* 2016 *Rev. Sci. Instrum.* **87** 11E327
[39] Hui Chen T *et al* 2017 *Phys. Plasmas* **24** 072715
[40] Perez F *et al* 2014 *Rev. Sci. Instrum.* **85** 11D613
[41] Hall T A 1984 *J. Phys. E: Sci. Instrum.* E **17** 110
[42] Martinolli E, Koenig M, Bourdenne J M and Perelli E 2004 *Rev. Sci. Instrum.* **75** 2024
[43] von Hamos L 1939 *Z. Kristallogr.* **101** 17
[44] Li X and Rosmej F B 2012 *Europhys. Lett.* **99** 33001
[45] Woolsey N C, Back C A, Lee R W, Calisti A, Mosse C, Stamm R, Talin B, Asfaw A and Klein L S 2000 *J. Quant. Spectrosc. Radiat. Transfer* **65** 573
[46] Li X, Rosmej F B, Lisitsa V S and Astapenko V A 2019 *Phys. Plasmas* **26** 033301
[47] Li X and Rosmej F B 2020 *Phys. Lett.* A **384** 126478
[48] Bitter M, Hill K W, Sauthoff N R, Efthimion P C, Meservey E, Roney W, von Goeler S, Horton R, Goldman M and Stodiek W 1979 *Phys. Rev. Lett.* **43** 129
[49] Casey D T *et al* 2018 *Phys. Plasmas* **25** 056308
[50] Sacks R, Tipton R and Graziani F 2016 *J. Phys.:Conf. Ser.* **717** 012076
[51] Dewald E L *et al* 2019 *Phys. Plasmas* **26** 072705
[52] Berzak Hopkins L *et al* 2018 *Phys. Plasmas* **25** 080706
[53] Beiersdorfer P *et al* 2019 *Phys. Rev.* A **100** 012511
[54] Hoarty D J *et al* 2013 *Phys. Rev. Lett.* **110** 265003
[55] Gu M F and Beiersdorfer P 2020 *Phys. Rev.* A **101** 032501
[56] Chrien R E, Klare K A and Murphy T J 1997 *Rev. Sci. Instrum.* **68** 607
[57] Zimmerman G and Kruer W 1975 *Plasma Phys. Control. Fusion* **11** 51
[58] Weizmann plasma formulary interactive (Available at: https://plasma-gate.weizmann.ac.il/pf/pf.html)
[59] Opachich Y P, Palmer N, Homoelle D, Hatch B, Bell P, Bradley D, Kalantar D, Browning D, Zuegel J and Landen O 2012 *Rev. Sci. Instrum.* **83** 125105